



저작자표시-비영리-변경금지 2.0 대한민국

이용자는 아래의 조건을 따르는 경우에 한하여 자유롭게

- 이 저작물을 복제, 배포, 전송, 전시, 공연 및 방송할 수 있습니다.

다음과 같은 조건을 따라야 합니다:



저작자표시. 귀하는 원저작자를 표시하여야 합니다.



비영리. 귀하는 이 저작물을 영리 목적으로 이용할 수 없습니다.



변경금지. 귀하는 이 저작물을 개작, 변형 또는 가공할 수 없습니다.

- 귀하는, 이 저작물의 재이용이나 배포의 경우, 이 저작물에 적용된 이용허락조건을 명확하게 나타내어야 합니다.
- 저작권자로부터 별도의 허가를 받으면 이러한 조건들은 적용되지 않습니다.

저작권법에 따른 이용자의 권리는 위의 내용에 의하여 영향을 받지 않습니다.

이것은 [이용허락규약\(Legal Code\)](#)을 이해하기 쉽게 요약한 것입니다.

[Disclaimer](#)

공학석사 학위논문

**Polyaniline Encapsulated Hollow Co-Fe
Prussian Blue Analogue Nanocubes
Modified on Polypropylene Separator to
Improve the Performance of
Lithium-sulfur Batteries**

폴리아닐린이 코팅된 중공성 코발트-철
프러시안 블루 아날로그 나노큐브 물질로
폴리프로필렌 분리막 표면 개질을 통한
리튬-황 전지의 성능 향상

2021년 8월

서울대학교 융합과학기술대학원

융합과학부 나노융합전공

조 학 래

**Polyaniline Encapsulated Hollow Co-Fe
Prussian Blue Analogue Nanocubes
Modified on Polypropylene Separator to
Improve the Performance of
Lithium-sulfur Batteries**

지도 교수 박 원 철

이 논문을 공학석사 학위논문으로 제출함
2021년 7월

서울대학교 융합과학기술대학원
융합과학부 나노융합전공
조 학 래

조학래의 공학석사 학위논문을 인준함
2021년 8월

위 원 장 _____

부위원장 _____

위 원 _____

**Polyaniline Encapsulated Hollow Co-Fe
Prussian Blue Analogue Nanocubes
Modified on Polypropylene Separator to
Improve the Performance of
Lithium–sulfur Batteries**

Hakrae Jo

Program in Nano Science and Technology

Graduate School of Convergence Science & Technology

Seoul National University

Abstract

In pursuit of high-energy-density and long-life lithium-sulfur (Li-S) batteries, it is greatly important to inhibit the shuttle effect of lithium polysulfides (LiPSs). In this work, hollow Co-Fe Prussian blue analogue nanocubes were prepared via oriented attachment. Polyaniline was further coated on the Co-Fe Prussian blue analogue nanocubes and modified on polypropylene separator for Li-S batteries. With a sulfur load of 60 %, the Li-S battery showed an initial capacitance of 723.1 mA h g⁻¹ at a current density of 1 A g⁻¹. The Li-S battery showed capacitance retention of 83.5 % after 100 cycles at a current density of 1 A g⁻¹. Moreover, the coulombic efficiency was maintained above 99.5% for all 100 cycles, indicating that there was an efficient ionic sieve that has a negligible effect on Li⁺ ion transport through the separator and prevents LiPSs from migrating to the anode. The material reported in this study shows potential to further improve the performance of Li-S batteries.

Keywords: lithium-sulfur battery; separator; hollow structure; Co-Fe Prussian blue analogue nanocubes; polyaniline;

Student Number: 2019-26495

Contents

1. Introduction	11
1.1. Lithium-Sulfur batteries.....	11
1.2. Sulfur/Carbon composites as cathode materials.....	12
1.3. MOFs/Conductive polymer separator in Li-S batteries.....	13
1.4. Motivation.....	14
 2. Experimental Section.....	16
2.1. Materials.....	16
2.2. Preparation of Co-Fe Prussian blue analogue.....	16
2.3. Synthesis of Co-Fe Prussian blue analogue@polyaniline	17
2.4. Synthesis of Modified Separator	17
2.5. Preparation of Li_2S_6 solution.....	18
2.6. Material characterization.....	18
2.7. Electrochemical measurements	19
2.8. Symmetric Cells for CV Analysis.....	22

3. Results and Discussion.....	23
3.1. Material analysis.....	23
3.2. Electrochemical analysis	36
 4. Conclusions.....	 42
 References.....	 43
 국문 초록 (Abstract in Korean).....	 53

List of Figures

Figure 1.	(a) TGA curve of CFP and CFP@PANI (b) TGA curve of KB/S composite.....	21
Figure 2.	Schematic illustration of the overall formation process of Co-Fe Prussian bl	
Figure 3.	(a) Low- and (b) high-magnification FE-SEM images of Co-l of CFP@PANI, (h) EDX elemental mapping (C, Co, Fe, N) of CFP@PANI.....	26
Figure 4.	XRD patterns of CFP@PANI and CFP.....	28
Figure 5.	Raman spectra of CFP@PANI and CFP.....	28
Figure 6.	FT-IR spectra of CFP@PANI and CFP.....	30
Figure 7.	(a) Nitrogen adsorption/desorption isotherms, (b) pore diameter distributions, and (c) adsorption tests of CFP/CFP@PANI and Blank with Li ₂ S ₆ . (d) XPS survey of CFP@PANI, (e) N 1s, (f) Co 2p, (g) Fe 2p. (h) Cross-sectional SEM image of CFP@PANI-PP. (I) Contact angle test.....	34
Figure 8.	(a) XPS survey of CFP, (b) C 1s, (c) N 1s, (d) Co 2p (e) Fe 2p.....	35
Figure 9.	C 1s of CFP@PANI.....	35
Figure 10.	(a) CV curves of the symmetric dummy cells employing	

CFP@PANI, CFP and PP separators at a scan rate of 10 mV s⁻¹. (b) Nyquist plots of the freshly prepared CFP@PANI and CFP separators before cycling. (c) Galvanostatic discharge/charge profiles of CFP@PANI, CFP, and KB electrode at current densities from 0.2 C. (d) CV curves of the cell using CFP@PANI separator at various scan rates from 0.1 to 1.0 mV s⁻¹. Plots of CV peak current of the (e) cathodic peak (Li₂S_x→Li₂S₂/Li₂S) and (f) anodic peak (Li₂S₂/Li₂S→Li₂S_x) against the square root of scan rate for the CFP@PANI and CFP separators. (g) Rate performance of CFP@PANI, CFP, and PP separators. (h) Long-term cycling performance of CFP@PANI, CFP, and KB electrodes at 1C for 100 cycles.....40

Figure 11. (a) CV curves of PP separator at various scan rates from 0.1 to 1.0 mV s⁻¹. Pl

1. Introduction

1.1. Lithium-Sulfur batteries

At the present stage, Lithium-ion batteries have become dominant power sources for a variety of portable electronic devices.[1,2] There is an urgent need from market to further improve the energy density of the electrochemical energy storage systems. Lithium-sulfur (Li-S) batteries with high theoretical specific capacity (1675 mA h g^{-1}) and specific energy density (2600 W h kg^{-1}) have attracted much attention for the next-generation energy storage systems. [3-6] In addition, sulfur is a highly abundant element while it is non-toxic and inexpensive, all of which serve as highly attractive features for cathode material. [3,7-9]

Still, Li-S batteries have several obstacles to overcome to be commercialized, such as the insulating nature of the discharge products (Li_2S and Li_2S_2), the volume expansion during charging and discharging (76%), and the well-known “shuttle effect” with caused by the solubility of lithium polysulfides (LiPSs) intermediates in the electrolyte. These problems result in low sulfur utilization, fast loss of capacity, severe self-discharge, and safety problems. [10,11]

1.2. Sulfur/Carbon composites as cathode materials

One of the most effective strategies for solving the problem of volume expansion and conductivity is to adopt nanostructure materials including porous carbons, [12,13] carbon nanotubes, [14,15] graphene, [16,17] and conductive polymer materials [18] as host materials to maintain the mechanical and electrical properties of the electrode. However, there are limitations to inhibit the shuttle of polysulfide only by physical adsorption to the nanostructure materials. [7] Because of this, incorporating catalytic effects by introducing well-engineered nanostructures has been proven to be effective in trapping the polysulfide. For example, metal oxides, [19,20] and metal-organic

frameworks (MOFs) [21,22] can efficiently inhibit the shuttle effect of polysulfides due to the electronegativity. The MOFs are also highly attractive materials to trap LiPSs due to their high porosity and excellent catalytic effect. [23] However, studies based on the cathode to inhibit the shuttle effect did not achieve satisfactory cycle stability. In addition, structural changes due to the volume expansion during the charging and discharging process further deteriorate the Li-S cathode performance. [24-27] The application of metal-based host materials to inhibit the LiPSs shuttle effect decreases the energy density since the metal-based host materials cannot make any contribution to capacity. Therefore, research on the development of new materials and advanced strategies that can not only suppressing the shuttle effect of LiPSs but also increase the sulfur loading on the cathode is highly desirable. [25]

1.3. MOFs/Conductive polymer separator in Li-S batteries

The separator is one of the important component Li-S battery, and the through interlayer between the cathode and the separator are the factor of improving the performance. Recently, studies in modification of separator have been increasingly conducted in parallel with the

advanced cathode design researches, as proven as a favorable and cost-effective approach to suppress the shuttle effect. Previous studies have shown that for high-performance Li-S batteries, an ideal modified separator should have the following advantages: 1) the material constituting the interlayer should have strong binding to LiPSs to effectively suppress the shuttle effect, 2) fast electron and ion transportability for high rate performance, and 3) appropriate thickness without scarifying the energy density. Additionally, the most important requirement is that the cathode materials, which do not affect the capacity, should be used as an interlayer material, while the cathode only retains the conductivity. In this respect, the modified separator with catalytic effect and electrostatic repulsion would be very attractive. [28-29] Catalytic effects accelerate the conversion kinetic of polysulfides so that a large amount of active material can be retained in the cathode. [4,28]

1.4. Motivation

Herein, this work report the performance improvement of Li-S battery by coating a celgard 2400 separator with hollow bimetallic Co-Fe Prussian blue analogue (CFP) encapsulated with polyaniline (PANI).

The CFP of high crystallinity was selected for separator material for the following reasons: high catalytic activity of Co ions and Fe ions, which increases the conversion kinetics of polysulfide; a large specific surface area due to its hollow structure, providing a wide active site and a pathway for lithium-ion; increases the conductivity of the precursor and inhibits the dissolution of polysulfide by chemical adsorption due to the (=N-) functional group in the backbone due to the PANI coating; the inhibition the shuttle effect by physical adsorption and increase the reactivation/reutilization of active materials. [24,30]

The constructed Li-S battery showed improved cycling performance and high rate performance using commercial ketjen black/sulfur (KB/S) cathodes. By using the CFP@PANI-PP separator, the cell exhibited a discharge capacity of 603.4 mA h g⁻¹ after 100 cycles with a capacity retention of 83.5%. The application of CFP@PANI-PP separator proves to be an effective strategy for improving the performance of Li-S batteries.

2. Experimental Section

2.1 Materials

Potassium hexacyanoferrate ($\text{K}_3\text{Fe}(\text{CN})_6$, 99 %), trisodium citrate dihydrate ($\text{C}_6\text{H}_5\text{Na}_3\text{O}_7 \cdot \text{H}_2\text{O}$, 99 %), and aniline ($\text{C}_6\text{H}_5\text{NH}_2$, 99.5 %) were purchased from Sigma-Aldrich Co., Cobalt(II) acetate tetrahydrate ($\text{C}_4\text{H}_6\text{CoO}_4 \cdot 4\text{H}_2\text{O}$, 98 %) was purchased from ACROS Co., hydrochloric acid (HCl , 35-37 %) was purchased from Samchun Co. Deionized (D.I) water was used in all the experiments. All chemicals were used as received without purification.

2.2 Preparation of Co-Fe Prussian blue analogue (CFP) [30]

The preparation of Co-Fe prussian blue analogue was followed the literature reported by David Lou et al. [30] In a typical synthesis, solution A was formed by 0.264 g of potassium hexacyanoferrate (**III**) dissolved in 120 mL of deionized water (D.I water). For solution B, 0.300 g of cobalt acetate tetrahydrate (**II**) and 0.294 g of trisodium citrate dehydrate were dissolved in 80 mL of D.I water. The resulting solution A was slowly added into solution B, followed by aging at 40 °C for 36 hours. The product was centrifuged and then washed with water and ethanol three times each, and finally dried at 60 °C in an

oven. [31]

2.3 Synthesis of Co-Fe Prussian blue analogue@polyaniline (CFP@PANI)

To a solution of the 30.0 mg of CFP in 10 mL of ethanol, was added 16.0 mL of 1 M HCl and 0.0456 mL of aniline. To this stirred solution, 28.5 mg of ammonium persulfate dissolved in 4 mL of 1 M HCl was added slowly by dropwise at 0 °C. The mixture was stirred for 4 hours, centrifuged and then washed with water three times each, and then freeze-dried. [32]

2.4 Synthesis of Modified Separators

To fabricate the modified separators, the as-prepared CFP@PANI composite was mixed with polyvinylidene fluoride (PVDF) binder in a ratio of 9:1 (w/w) in N-methyl-2-pyrrolidinone (NMP) at a concentration of 1 mg mL⁻¹. After ultrasonicated under continuous stirring, the homogeneous suspension was vacuum filtered onto a commercial polypropylene (PP) separator (celgard 2400). The CFP@PANI modified separator was obtained after drying overnight in a 60 °C vacuum oven, and the mass loading of CFP@PANI on the separator surface was about 0.2 mg cm⁻². The separator was finally

punched into disks with a diameter of 19 mm for subsequent assembly of the Li-S battery. For comparison, the CFP modified separators were prepared by following the identical method, and the coating interlayer on PP separator was controlled with the same mass loading. [11]

2.5 Preparation of Li_2S_6 solution

A 0.2 M Li_2S_6 solution was obtained by dissolving the S and Li_2S with a molar ratio of 5:1 in a mixed solvent of 1,3-dioxolane (DOL)/1,2-dimethoxyethane (DME) with a ratio of 1:1 (v/v) under stirring at 60 °C for 24 hours in the glovebox. To prepare 8 mM LiPSs, 200 μL of 0.2 M polysulfide solution was added to 4.8 mL of electrolyte. [4]

2.6 Material characterization

Morphological and structural of CFP@PANI and CFP were characterized by using field emission transmission electron microscopy (FE-TEM, JEM-2010, JEOL) equipped with an energy-dispersive X-ray (EDX) spectrum and field emission scanning electron microscope (FE-SEM, Hitachi S-4800). The X-ray photoelectron spectroscopy (XPS) analysis was performed on XPS (AXIS-HIS, Kratos Analytical)

by using Mg K α X-ray source. The Raman spectrum was obtained by using a Raman spectrometer (DXR2xi Raman Imaging Microscope, Thermo Scientific) with an excitation laser wavelength of 532 nm. N₂ adsorption-desorption was collected by using an adsorption analyzer (BELSORP-mini II, MicrotracBEL Corp.). The crystal structure of the sample was characterized by using X-ray diffractometer (D8 Advanced, Bruker) with Cu K α ($\lambda = 1.5406$ Å) radiation. Thermogravimetric analysis (TGA) using a thermal analyzer (TGA/DSC 1, Mettler Toledo Co.) was operated at a heating rate of 10 °C min⁻¹ under in nitrogen or air atmosphere.

2.7 Electrochemical measurements

The KB/S composite was prepared by mixing the ketjen black and sulfur in a mass ratio of 3:6 at 160 °C for 12 hours in a sealed reactor. According to thermogravimetric analysis, the sulfur content of the KB/S composite was measured to be 66.6 % (**Figure 1**, Supporting Information). To prepare the working cathode, the KB/S composite was mixed with PVDF and NMP in a mass ratio of 6:3:1. [28] Afterwards, the slurry was casted onto a carbon coated aluminum foil using a doctor blade, and dried in a vacuum oven at 50 °C overnight. The electrodes

were obtained by punching the composite loaded Al foil into disks with a diameter of 12 mm, and the sulfur loading in the cathode was approximately 0.8–1.0 mg cm⁻². To prepare the electrolyte solution, 1.0 M of Bis (trifluoromethane) sulfonamide (LiTFSI) lithium salt was dissolved in a mixture solvent of DOL and DME with a 1:1 ratio (v/v) and 1wt % of LiNO₃ salt was added as additive. The electrochemical performance was tested with a 2032-coin cell using Li metal as counter and reference electrodes and PP, CFP-PP, or CFP@PANI-PP as separator. The amount of electrolyte was fixed at 30 μL mg⁻¹ for cells with prepared sulfur content of 1 mg. The coin cell was assembled in an Ar-filled glove box with a moisture and oxygen content of less than 1 ppm. Galvanostatic electric charge and discharge tests were performed by using a WBCS3000S cyclor (WonATech Co.) at different current densities in the voltage range of 1.7-2.8 V (vs. Li/Li⁺). Cyclic voltammetry (CV) was measured from 1.7 to 2.8 V (vs. Li/Li⁺) at various scan rates from 0.1 to 1.0 mV s⁻¹. Electrochemical impedance spectroscopy (EIS) was performed by using a ZIVE SP1 electrometer (ZIVE LAB, WonATech Co.) in frequency range from 100 kHz to 0.1 Hz.

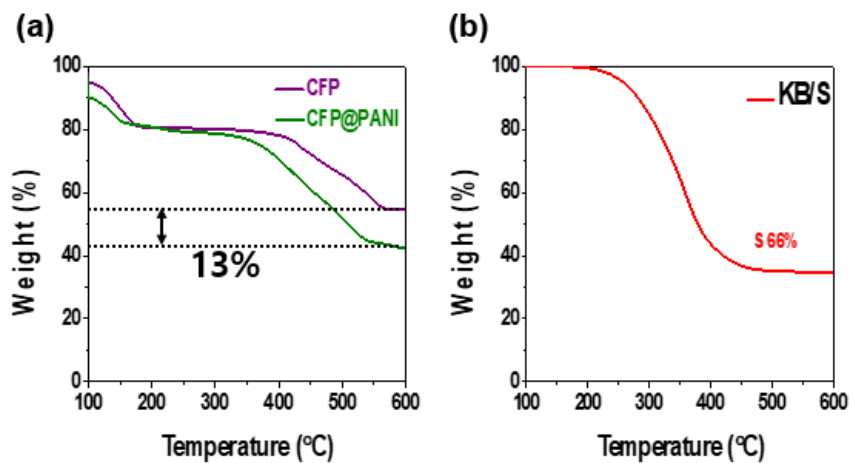


Figure 1. (a) TGA curves of CFP and CFP@PANI. (b) TGA curve of KB/S composite.

2.8 Symmetric Cells for CV Analysis

To prepare electrodes for symmetric cells, PVDF binder was added to CFP@PANI or CFP in an NMP solvent at a weight ratio of 9:1 to prepare slurry and then coated on Al current collector. The CFP@PANI (or CFP) load at the electrode was approximately 1 mg. Two identical electrodes were assembled into a standard 2032-coin cell with 2400 separator of Celgard (<0.1 ppm for oxygen). 30 μL electrolyte containing 0.1 M Li_2S_6 and 1 M LiTFSI dissolved in DOL/DME (v/v = 1/1) was added to the cell. The CV data of the symmetric cells was obtained on a WBCS3000S cycler (WonAtech Co.). The voltage range of CV measurement was from -1.0 to 1.0 V at various scan rates from 1.0 to 5.0 mV s^{-1} .

3. Results and Discussion

3.1 Material analysis

Figure 2 represents the schematic diagram for the preparation of Co-Fe Prussian blue analogue@polyaniline-polypropylene (CFP@PANI-PP). Briefly, CFP cage/frame-like structure was prepared by stirring a mixture of cobalt (II) acetate, potassium hexacyanoferrate (III), and trisodium citrate water solution for 5 minutes, followed by aging at 40 °C for 36 hours. [30] In this process, trisodium citrate dihydrate acts as a chelating agent, results in the formation of a metal-organic framework architecture of CFP.

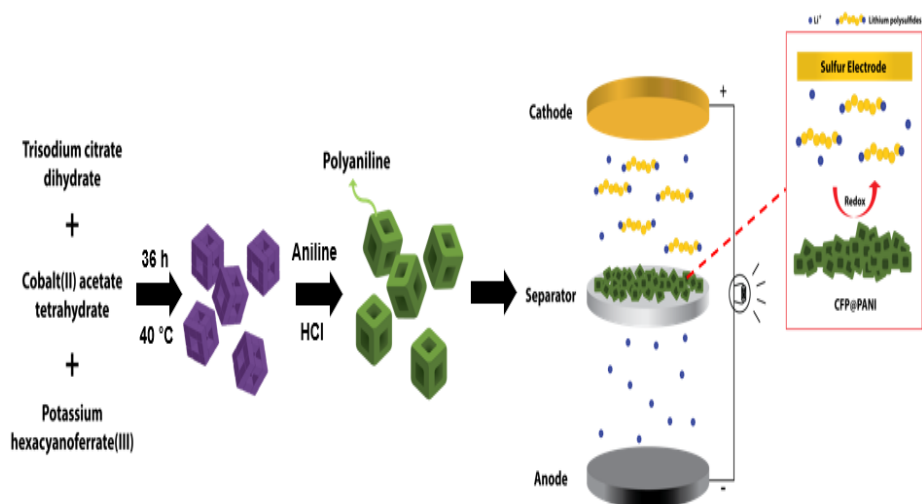


Figure 2. Schematic illustration of the overall formation process of Co-Fe Prussian blue analogue@polyaniline-polypropylene (CFP@PANI-PP).

The synthesized CFP possesses a uniform hollow structure with a size distribution of 350 nm as shown in **Figures 3a and 3b**. In addition, TEM image shown **Figure 3c** reviews that the synthesized CFP is polycrystalline with a block alignment structure. Elemental mapping results are shown in **Figure 3d** which were taken by EDX to confirm the elemental distribution of Fe, Co, C, N and O in CFP. [31] The block-aligned structure could increase the movement and freedom of CFP, which might improve the cycling stability. Moreover, frame/cage-like structure has higher crystallinity than single crystals, resulting in high catalytic activity. Finally, the obtained CFP was coated with aniline for 4 hours using HCl as a solvent. Finally, CFP@PANI was coated on celgard 2400 with a vacuum filter. The surface morphology of CFP@PANI (**Figures 3e and 3f**) was investigated by SEM. These images show that PANI was coated on CFP.

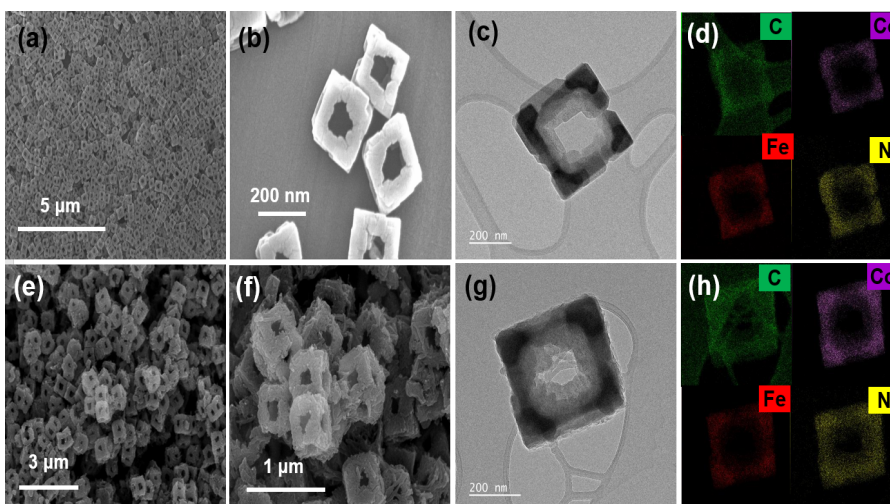


Figure 3. (a) Low- and (b) high-magnification FE-SEM images of Co-Fe Prussian blue analogue (CFP), (c) FE-TEM images of CFP and (d) EDX elemental mapping (C, Co, Fe, N) of CFP. (e) Low- and (f) high-magnification FE-SEM images of Co-Fe Prussian blue analogue@polyaniline (CFP@PANI), (g) FE-TEM images of CFP@PANI, (h) EDX elemental mapping (C, Co, Fe, N) of CFP@PANI.

XRD data of each samples was summarized in **Figure 4**. The three diffraction peaks of CFP and CFP@PANI at $2\theta = 17.71^\circ, 25.36^\circ, 35.85^\circ$ indicates the (200), (220), and (400) planes, respectively. The (200) plane with the highest intensity is the fcc crystal structure of CFP, which means that CFP is structurally stable. Besides, by comparing CFP and CFP@PANI XRD peaks, it was observed that there was no change and that the structure and crystallinity were not affected even under acid conditions. [30,33-34] Raman spectra are recorded to confirm the presence of PANI in CFP@PANI. As shown in **Figure 5**, for CFP, a low intensity peak exists widely from 320.49 cm^{-1} to 638.79 cm^{-1} . In addition, several typical characteristic peaks are detected in the CFP@PANI sample. The peak centers at 1161.39 and 1213.22 cm^{-1} can be further assigned to the C-H bending vibration of quinoid rings and benzenoids. [35] The peaks at 1494.17 and 1584.18 cm^{-1} are associated with the vibration of additional C=N groups and the C=C organization of the benzene ring. [36-37] However, the normal peak shifted from CFP and weakened, which is due to CFP and PANI species interactions. Consequently, the Raman results provide evidence supporting the successful synthesis of CFP@PANI nanostructures. [24]

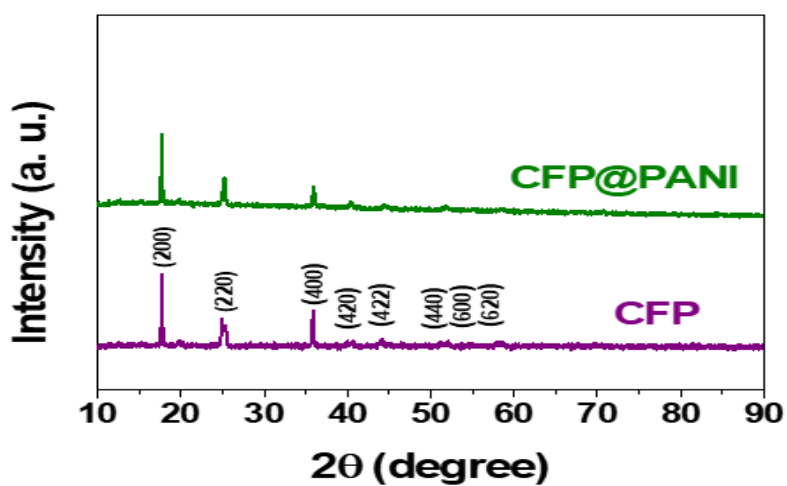


Figure 4. XRD patterns of CFP@PANI and CFP.

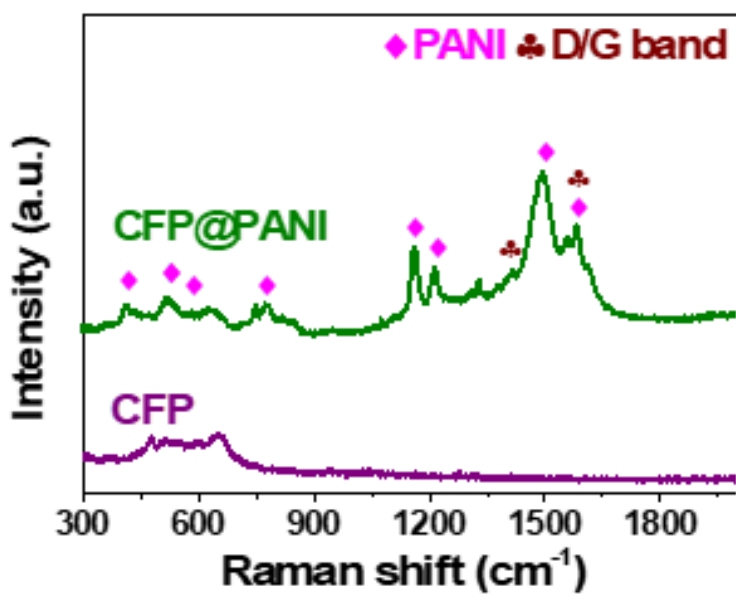


Figure 5. Raman spectra of CFP@PANI and CFP.

FT-IR was performed to identify chemical bonds in CFP and CFP@PANI nanostructure. The CFP@PANI sample (**Figure 6**) shows five characteristic peaks at 1118, 1245, 1301, 1496, and 1579 cm^{-1} . The peaks located at 1302 cm^{-1} is recorded for C-H bending vibrations of aromatic amines and C-N stretching vibrations of benzenoid rings. [38] The peak at 1245 cm^{-1} is related to the C=N stretching mode of the PANI chain. [39] The peak located at 2075 cm^{-1} is a characteristic stretching vibration of cyanide in $\text{Co(II)-N}\equiv\text{C-Fe(II)}$. The absorption peaks at 3629, 3370 and 1579 cm^{-1} are O-H stretching vibrations associated with H_2O stretching vibrations and bending the two peaks located at 1496 and 1579 cm^{-1} can be attributed to stretching vibration of benzene(N-B-N) and quinone(N=Q=N) in PANI. [40] In addition, the FT-IR spectrum of CFP@PANI shows four additional absorption peaks of PANI compared to the CFP sample, showing the PANI coating. Overall, FT-IR characterization provides evidence that PANI was successfully encapsulated with CFP surface.

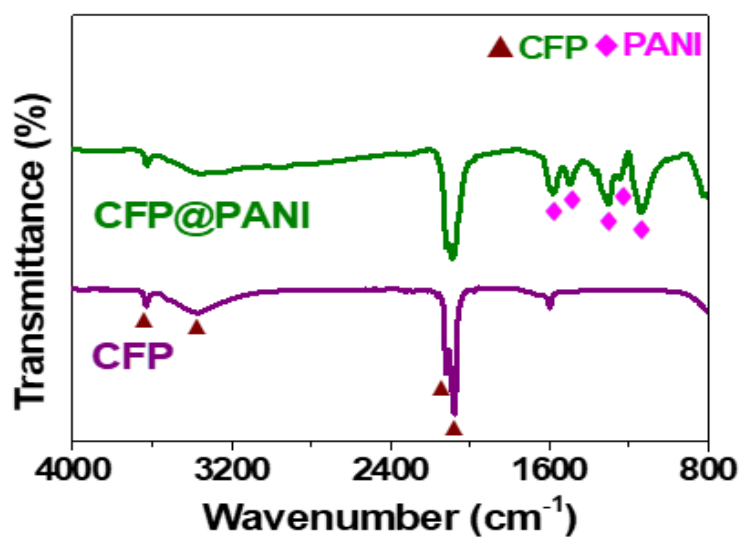


Figure 6. FT-IR spectra of CFP@PANI and CFP.

To further characterize surface area and porosity of the material, N₂ adsorption-desorption measurements were also performed (**Figure 7a & 7b**). CFP@PANI (52.269 m² g⁻¹) has a higher surface area than that of CFP (46.332 m² g⁻¹). Moreover, it can be seen from the data that CFP@PANI possesses more mesopores and macropores, which means that the active site increases. These data indicate that PANI coating increases the active sites for reaction with polysulfide. For verifying the chemical affinity of the synthetic material to LiPSs, a Li₂S₆ adsorption test was performed by using UV-vis absorption spectroscopy applying a Li₂S₆ solution by monitoring the concentration of Li₂S₆. As shown in **Figure 7c** the 8mM Li₂S₆ solution containing CFP@PANI became almost colorless after 24h, showing a significantly reduced absorption peak in the visible range, whereas the Li₂S₆ solution containing CFP showed a bright yellow color. Soluble LiPSs are partially trapped by CFP due to chemical absorption to metal (Co, Fe) and nitrogen, but the catalytic effect of CFP itself is insufficient to trap most of LiPSs. In contrast, for CFP@PANI, a strong chemical bond with LiPSs is possible due to =N- in the backbone. In addition, the dissolution of LiPSs can be inhibited with CFP inside the thinly coated PANI. [41-42]

X-ray photoelectron spectroscopy (XPS) was performed to

demonstrate the elemental valence of the CFP and CFP@PANI presented in **Figure 7d-g**, **Figure 8** and **Figure 9**. The survey spectra suggest the coexistence of C, N, O, Fe and Co elements in CFP. **(Figure 8)** The high-resolution C 1s XPS spectra show different bonding structures and main bonding structures are attributed to C-C, C-N, C=O, C-M. The peaks at 284.6, 285.2, 286.3, 288.6 eV suggest the binding of CFP to the cynde group and metal, respectively. In C 1s of CFP@PANI, C=C, C-C and C-N bonds were observed at 283.7, 284.6, and 285.6 eV, which resulted in the disappearance of weak metal peaks compared to CFP and the prominent peak of PANI. [43] **Figure 7e** the high-resolution N 1s XPS spectra of CFP@PANI show 397.0, 398.0 and 399.7 eV, which can be assigned to pyridine N, pyrrole N, and graphitic N bonds, respectively. In the case of pyridine N, it inhibits the dissolution through strong adsorption with polysulfide, suggesting that PANI coating with high intensity pyridine N effectively inhibits dissolution of polysulfide. [44] In addition, high-resolution Co 2p spectra can be usually divided into $2p^{3/2}$ (781.7 eV) and $2p^{1/2}$ (797.4 eV) peak energy states coupled from spin-orbitals. The two peaks at 787.4 and 804.6 eV are satellite peaks. These rotational orbital splits (15.7 eV) and Shake-up satellites (Sat.) imply an oxidation state (Co^{2+})

in Co-NC. **(Figure 7f)** [45-46] For Fe, the high-resolution Fe 2p spectrum **(Figure 7g)** show five constituent peaks. Peak located at 707.8 ($2p^{3/2}$) and 720.7 eV ($2p^{1/2}$) are indexed to Fe^{2+} and Fe-CN bonds. The last (716.4 eV) is indicating satellites peak. Most importantly, CFP@PANI exhibits a strong peak intensity of the oxidation state of Fe^{3+} . This means that the H_2O bond-forming coordination bond with Fe is broken under acid conditions and Fe is arranged in a stable state. On the other hand, in CFP, the intensity peak of the oxidation state of Fe^{3+} is very weak. This implies a large presence of unstable Fe^{2+} and many H_2O coordination bonds to CFP. The coordination state disrupts the electrochemical of CFP and disrupts its structural stability. **(Figure 8e)** [47] The cross-sectional SEM image is $\sim 7\ \mu m$ thick at CFP@PANI. **(Figure 7h)** For thin coating on PP separator dispersibility with solvent and properties of material are important. CFP@PANI, which is highly hydrophilic, is thinly coated on PP and has the advantage of lithium-ion penetration throughout CFP@PANI due to its improved wettability. **(Figure 7I)** [24] From the thermogravimetric analysis (TGA) curve in **Figure 1** it can be inferred that the content of PANI is 13wt % and the sulfur content and areal sulfur loading of the KB/S cathode electrode are up to 60% and 0.8 –

1.0 mg cm⁻², respectively.

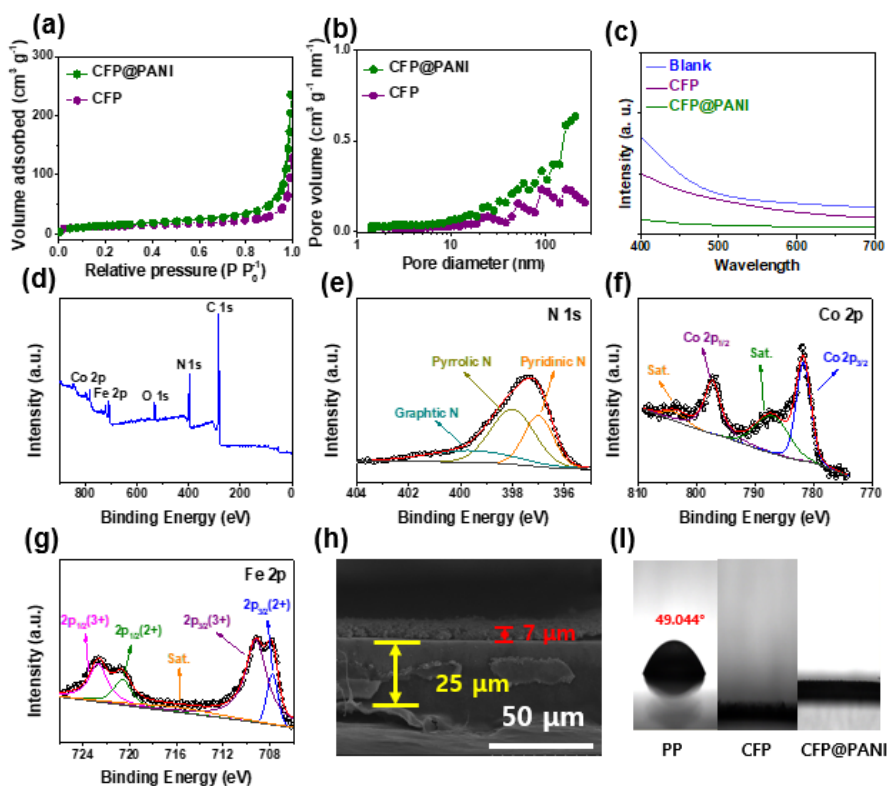


Figure 7. (a) Nitrogen adsorption/desorption isotherms, (b) pore diameter distributions, and (c) adsorption tests of CFP/CFP@PANI and Blank with Li₂S₆. (d) XPS survey of CFP@PANI, (e) N 1s, (f) Co 2p, (g) Fe 2p, (h) Cross-sectional SEM image of CFP@PANI-PP. (i) Contact Angle test.

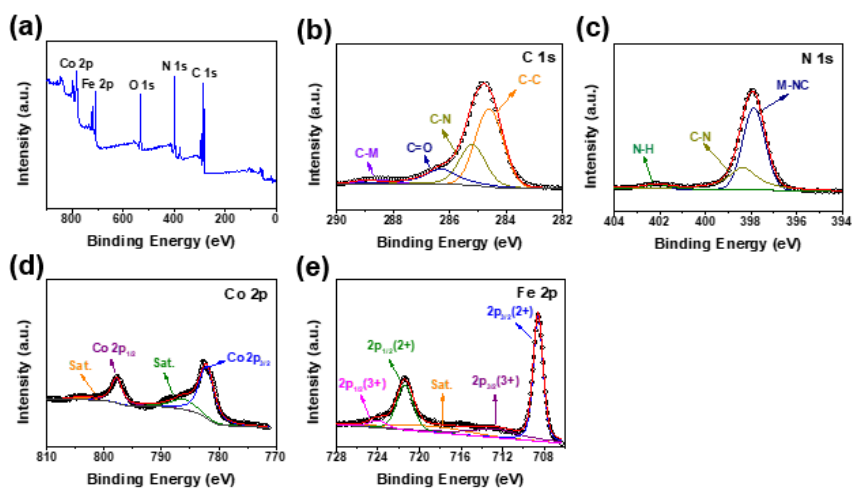


Figure 8. (a) XPS survey of CFP, (b) C 1s, (c) N 1s, (d) Co 2p (e) Fe 2p.

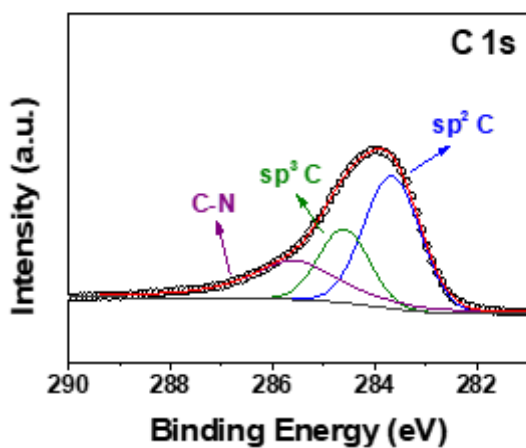


Figure 9. C 1s of CFP@PANI.

3.2. Electrochemical analysis

CFP@PANI as shown in **Figure 10a** clarifies the kinetics that accelerate the redox kinetics of Li_2S_x to low-grade LiPSs in the symmetric cell. Almost identical CV curves were observed for different cycles, suggesting facile redox kinetics of CFP@PANI at high rates. [4] **Figure 10b** shows electrochemical impedance spectroscopy (EIS) plots of fresh cell CFP and CFP@PANI interlayer. Typically, high frequencies of the semicircle come from the charge transfer resistance (R_{ct}) and the slanted line at low frequencies related to the lithium diffusion process within the Warburg impedance. Clearly, cells with CFP@PANI interlayer perform much lower R_{ct} than cells with CFP separators, indicating that the interlayer has fast charge transfer capabilities and can accelerate electron transport as additional upper current collectors. [48] The galvanostatic charge and discharge curves of CFP@PANI, CFP, and KB were summarized in **Figure 4c**. Two typical voltage plateau of both as-prepared samples at around 2.3 V and 2.1 V attribute to the S_8 convert to polysulfide and further to Li_2S during the discharge process, and the corresponding typical voltage plateau present the conversion of Li_2S to S_8 during the charge process, which are consistent with the results of CV curves. These results

indicate that the redox process that $\text{Li}_2\text{S}_8/\text{Li}_2\text{S}_6$ converted to Li_2S is accelerated due to the catalytic effect. To assess the electrochemical performance of the resulting Li-S cells CFP@PANI-PP and CFP-PP, PP a 2032-type coin cell was fabricated. CV curves show a markedly decreasing reduction peak with slope = -155, CFP slope = -128 and PP = -45 for CFP@PANI in cathodic scans (peak and C2) and CFP in anodic scans. CFP@PANI showed an increasing oxidation peak (peak A) with slope = 381, CFP = 376 and PP = 218 (**Figures 10e, 10f and 11**) [49]. According to the Randles-Sevcik equation, the peak current (I_p) and the scan rate (v) have the following relationship:

$$I_p = (2.69 \times 10^5) n^{1.5} A D_{\text{Li}}^{0.5} C_{\text{Li}} v^{0.5}$$

where I_p is the peak current, n is the number of electrons, A is the surface area of the electrode, D_{Li} is the Li-ion diffusion coefficient, C_{Li} is the Li-ion concentration in the electrolyte, and v is the scan rate. The cathodic and anodic D_{Li} values of the two electrodes are calculated from the linear relationship of I_p vs. $v^{0.5}$, as compared in **Figure 4e and 4f**.⁵⁰ The CFP@PANI-PP exhibits a steeper slope than CFP-PP in both the cathodic peaks and anodic peaks, which results in the faster charge transfer and higher lithium ion diffusivity of PANI, thus providing a faster rate during cycling. The rate performance of

CFP@PANI-PP, CFP-PP and PP separators are analyzed at current densities from 0.2 C to 1 C as shown in **Figure 4g**. The CFP @ PANI-pp separator exhibits excellent specific discharge capacities of 1070.0, 880.3 and 790.6 mA h g⁻¹ at high current densities of 0.2, 0.5 and 1 C, respectively. The CFP-PP separator has a lower specific discharge capacity compared to the CFP@PANI-PP. The reinforced rate capacity of the CFP@PANI-PP separator is attributed to the presence of CFP nanostructure and PANI, which enables a rapid LiPSs redox reaction, as explained in the symmetric cell CV and EIS results. In addition, the discharge capacity of the CFP@PANI-PP separator recovered to 975.3 mA h g⁻¹ when the current density was returned to 0.2 C, suggesting the excellent structural stability of the CFP@PANI-PP composite. The corresponding charge/discharge profile of the sample is shown in **Figure 4g**. On the other hand, at high current densities of 0.5 C and 1.0 C, these stabilizers are not observed in the PP separator due to the slow kinetics of LiPSs transformation. **Figure 4h** shows the long-term cycling performance of CFP@PANI-PP, CFP-PP and PP separators evaluated in 1.0 C. The CFP@PANI separator indicates the best cycling stability with a high discharge capacity of 603.3 mA h g⁻¹ after 100 cycles with a capacity retention of 83.5 %. However, the CFP-PP

separator has a discharge capacity of 560.86 mA h g⁻¹ after 100 cycles with a low-capacity retention rate of 74.1 % due to its low chemical affinity with LiPSs. Co and Fe of CFP can inhibit the dissolution of LiPSs due to their catalytic effect, but they do not have a functional group that can inhibit dissolution, resulting in severe capacity degradation. These results show that the CFP@PANI-PP separator not only immobilize LiPSs with strong chemical affinity, but also provides high Li⁺ diffusivity, resulting in improved long-term cycling performance.

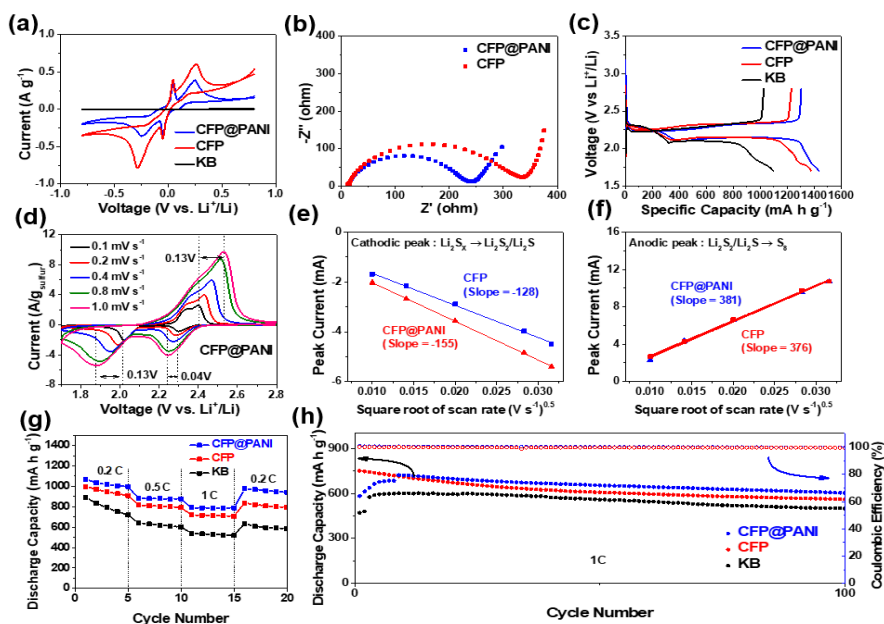


Figure 10. (a) CV curves of the symmetric dummy cells employing CFP@PANI, CFP and PP separators at a scan rate of 10 mV s⁻¹. (b) Nyquist plots of the freshly prepared CFP@PANI and CFP separators before cycling. (c) Galvanostatic discharge/charge profiles of CFP@PANI, CFP, and KB electrode at current densities from 0.2 C. (d) CV curves of the cell using CFP@PANI separator at various scan rates from 0.1 to 1.0 mV s⁻¹. Plots of CV peak current of the (e) cathodic peak ($\text{Li}_2\text{S}_x \rightarrow \text{Li}_2\text{S}_2/\text{Li}_2\text{S}$) and (f) anodic peak ($\text{Li}_2\text{S}_2/\text{Li}_2\text{S} \rightarrow \text{Li}_2\text{S}_x$) against the square root of scan rate for the CFP@PANI and CFP separators. (g) Rate performance of CFP@PANI, CFP, and PP separators. (h) Long-term cycling performance of CFP@PANI, CFP, and KB electrodes at 1C for 100 cycles.

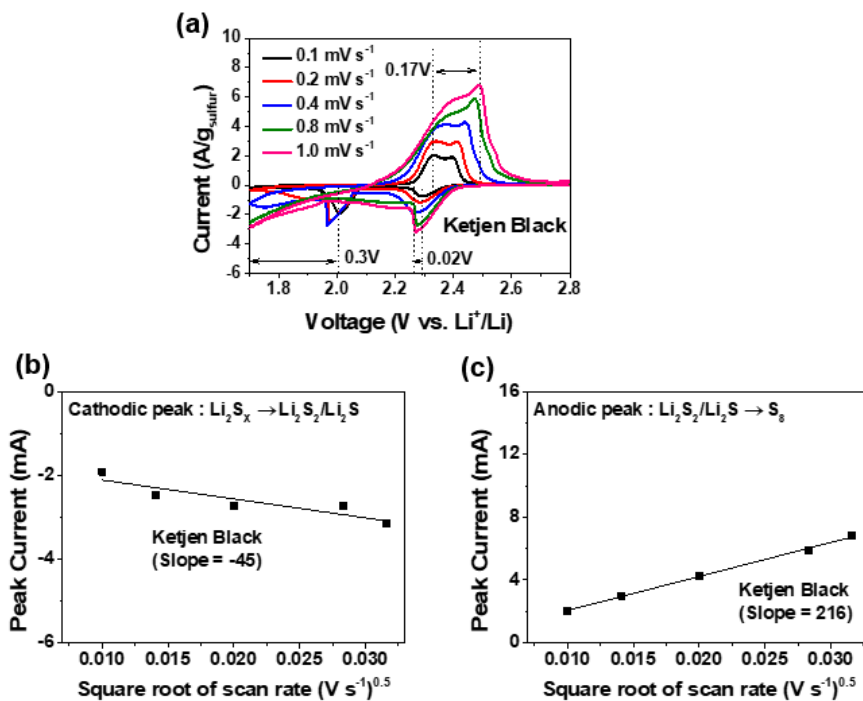


Figure 11. (a) CV curves of PP separator at various scan rates from 0.1 to 1.0 mV s⁻¹. Plots of CV peak current of the (b) cathodic peak ($\text{Li}_2\text{S}_x \rightarrow \text{Li}_2\text{S}_2/\text{Li}_2\text{S}$) and (c) anodic peak ($\text{Li}_2\text{S}_2/\text{Li}_2\text{S} \rightarrow \text{Li}_2\text{S}_x$) against the square root of scan rate for the PP separator.

4. Conclusions

In summary, hollow Co-Fe Prussian blue analogue nanocubes were prepared via oriented attachment and adopt as the interlayer material for the widely employed KB/S cathodes. The CFP@PANI surface is proved to be LiPSs affinities via both strong chemical bonding. With a sulfur load of 60 %, the Li-S battery showed an initial capacitance of 723.1 mA h g⁻¹ at a current density of 1 A g⁻¹. The Li-S battery showed capacitance retention of 83.5 % after 100 cycles at a current density of 1 A g⁻¹. Moreover, the coulombic efficiency was maintained above 99.5% for all 100 cycles, indicating that there was an efficient ionic sieve that has a negligible effect on Li⁺ ion transport through the separator and prevents LiPSs from migrating to the anode. The material reported in this study shows potential to further improve the performance of Li-S batteries.

References

- [1] Armand, M.; Tarascon, J. M. Building better batteries. *Nat.* **2008**, *451*, 652-657.
- [2] Arico, A. S.; Bruce, P.; Scrosati, B.; Tarascon, J. M.; Van Schalkwijk, W. Nanostructured materials for advanced energy conversion and storage devices. *Nat. Mater.* **2005**, *4*, 366-377.
- [3] Manthiram, A.; Fu, Y. Z.; Chung, S. H.; Zu, C. X.; Su, Y. S. Rechargeable Lithium-Sulfur Batteries. *Chem. Rev.* **2014**, *114*, 11751-11787.
- [4] Wu, Q. P.; Zhou, X. J.; Xu, J.; Cao, F. H.; Li, C. L. Adenine Derivative Host with Interlaced 2D Structure and Dual Lithiophilic-Sulfiphilic Sites to Enable High-Loading Li-S Batteries. *Acs Nano.* **2019**, *13*, 9520-9532.
- [5] Balach, J.; Jaumann, T.; Klose, M.; Oswald, S.; Eckert, J.; Giebeler, L. Functional Mesoporous Carbon-Coated Separator for Long-Life, High-Energy Lithium-Sulfur Batteries. *Adv. Funct. Materials.* **2015**, *25*, 5285-5291.
- [6] Eshetu, G. G.; Judez, X.; Li, C. M.; Martinez-Ibanez, M.; Gracia, I.; Bondarchuk, O.; Carrasco, J.; Rodriguez-Martinez, L. M.; Zhang, H.; Armand, M. Ultrahigh Performance All Solid-State Lithium Sulfur

Batteries: Salt Anion's Chemistry-Induced Anomalous Synergistic Effect. *J. Am. Chem. Soc.* **2018**, *140*, 9921-9933.

[7] Deng, C.; Wang, Z. W.; Wang, S. P.; Yu, J. X. Inhibition of polysulfide diffusion in lithium-sulfur batteries: mechanism and improvement strategies. *J. Mater. Chem. A*. **2019**, *7*, 12381-12413.

[8] Wang, J. G.; Xie, K. Y.; Wei, B. Q. Advanced engineering of nanostructured carbons for lithium-sulfur batteries. *Nano Energy*. **2015**, *15*, 413-444.

[9] Ji, X. L.; Nazar, L. F. Advances in Li-S batteries. *J. Mater. Chem. A*. **2010**, *20*, 9821-9826.

[10] Mikhaylik, Y. V.; Akridge, J. R. Polysulfide shuttle study in the Li/S battery system. *J. Electrochem. Soc.* **2004**, *151*, A1969-A1976.

[11] Sun, J.; Sun, Y. M.; Pasta, M.; Zhou, G. M.; Li, Y. Z.; Liu, W.; Xiong, F.; Cui, Y. Entrapment of Polysulfides by a Black-Phosphorus-Modified Separator for Lithium-Sulfur Batteries. *Adv. Mater.* **2016**, *28*, 9797-9803.

[12] Zhu, Q. Z.; Zhao, Q.; An, Y. B.; Anasori, B.; Wang, H. R.; Xu, B. Ultra-microporous carbons encapsulate small sulfur molecules for high performance lithium-sulfur battery. *Nano Energy*. **2017**, *33*, 402-409.

[13] Hu, L.; Lu, Y.; Li, X. N.; Liang, J. W.; Huang, T.; Zhu, Y. C.;

Qian, Y. T. Optimization of Microporous Carbon Structures for Lithium-Sulfur Battery Applications in Carbonate-Based Electrolyte.

Small. **2017**, *13*, 1603533.

[14] Jin, F. Y.; Xiao, S.; Lu, L. J.; Wang, Y. Efficient Activation of High-Loading Sulfur by Small CNTs Confined Inside a Large CNT for High-Capacity and High-Rate Lithium-Sulfur Batteries. *Nano Lett.* **2016**, *16*, 440-447.

[15] Zheng, M. B.; Chi, Y.; Hu, Q.; Tang, H.; Jiang, X. L.; Zhang, L.; Zhang, S. T.; Pang, H.; Xu, Q. Carbon nanotube-based materials for lithium-sulfur batteries. *J. Mater. Chem. A*. **2019**, *7*, 17204-17241.

[16] Yu, M. P.; Li, R.; Wu, M. M.; Shi, G. Q. Graphene materials for lithium-sulfur batteries. *Energy Storage Mater.* **2015**, *1*, 51-73.

[17] Papandrea, B.; Xu, X.; Xu, Y. X.; Chen, C. Y.; Lin, Z. Y.; Wang, G. M.; Luo, Y. Z.; Liu, M.; Huang, Y.; Mai, L. Q.; Duan, X. F. Three-dimensional graphene framework with ultra-high sulfur content for a robust lithium-sulfur battery. *Nano Res.* **2016**, *9*, 240-248.

[18] Li, Y. R.; Yuan, L. X.; Li, Z.; Qi, Y. Z.; Wu, C.; Liu, J.; Huang, Y. H. Improving the electrochemical performance of a lithium-sulfur battery with a conductive polymer-coated sulfur cathode. *Rsc Adv.*

2015, 5, 44160-44164.

[19] Kim, M.; Lee, J.; Jeon, Y.; Piao, Y. Phosphorus-doped graphene nanosheets anchored with cerium oxide nanocrystals as effective sulfur hosts for high performance lithium-sulfur batteries. *Nanoscale*. **2019**, 11, 13758-13766.

[20] Sun, Q.; Xi, B. J.; Li, J. Y.; Mao, H. Z.; Ma, X. J.; Liang, J. W.; Feng, J. K.; Xiong, S. L. Nitrogen-Doped Graphene-Supported Mixed Transition-Metal Oxide Porous Particles to Confine Polysulfides for Lithium-Sulfur Batteries. *Adv. Energy Mater.* **2018**, 8, 1800595.

[21] Zhang, H.; Zhao, W. Q.; Wu, Y. Z.; Wang, Y. S.; Zou, M. C.; Cao, A. Y. Dense monolithic MOF and carbon nanotube hybrid with enhanced volumetric and areal capacities for lithium-sulfur battery. *J. Mater. Chem. A*. **2019**, 7, 9195-9201.

[22] Zheng, Y.; Zheng, S. S.; Xue, H. G.; Pang, H. Metal-organic frameworks for lithium-sulfur batteries. *J. Mater. Chem. A*. **2019**, 7, 3469-3491.

[23] Hong, X. J.; Song, C. L.; Yang, Y.; Tan, H. C.; Li, G. H.; Cai, Y. P.; Wang, H. X. Cerium Based Metal-Organic Frameworks as an Efficient Separator Coating Catalyzing the Conversion of Polysulfides for High

Performance Lithium-Sulfur Batteries. *Acs Nano*. **2019**, *13*, 1923-1931.

[24] Tao, X. Y.; Wang, J. G.; Liu, C.; Wang, H. T.; Yao, H. B.; Zheng, G. Y.; Seh, Z. W.; Cai, Q. X.; Li, W. Y.; Zhou, G. M.; Zu, C. X.; Cui, Y. Balancing surface adsorption and diffusion of lithium-polysulfides on nonconductive oxides for lithium-sulfur battery design. *Nat. Commun*. **2016**, *7*.

[25] Ghazi, Z. A.; He, X.; Khattak, A. M.; Khan, N. A.; Liang, B.; Iqbal, A.; Wang, J. X.; Sin, H. S.; Li, L. S.; Tang, Z. Y. MoS₂/Celgard Separator as Efficient Polysulfide Barrier for Long-Life Lithium-Sulfur Batteries. *Adv. Mater*. **2017**, *29*, 1606817.

[26] Zhou, G. M.; Li, L.; Wang, D. W.; Shan, X. Y.; Pei, S. F.; Li, F.; Cheng, H. M. A Flexible Sulfur-Graphene-Polypropylene Separator Integrated Electrode for Advanced Li-S Batteries. *Adv. Mater*. **2015**, *27*, 641-647.

[27] Huang, J. Q.; Zhuang, T. Z.; Zhang, Q.; Peng, H. J.; Chen, C. M.; Wei, F. Permselective Graphene Oxide Membrane for Highly Stable and Anti-Self-Discharge Lithium-Sulfur Batteries. *Acs Nano*. **2015**, *9*, 3002-3011.

[28] Cheng, P.; Guo, P. Q.; Sun, K.; Zhao, Y. G.; Liu, D. Q.; He, D. Y.

CeO₂ decorated graphene as separator modification material for capture and boost conversion of polysulfide in lithium-sulfur batteries. *J. Membrane. Sci.* **2021**, *619*, 118780.

[29] Hao, Z. X.; Yuan, L. X.; Li, Z.; Liu, J.; Xiang, J. W.; Wu, C.; Zeng, R.; Huang, Y. H. High performance lithium-sulfur batteries with a facile and effective dual functional separator. *Electrochim. Acta* **2016**, *200*, 197-203.

[30] Nai, J. W.; Guan, B. Y.; Yu, L.; Lou, X. W. Oriented assembly of anisotropic nanoparticles into frame-like superstructures. *Sci. Adv.* **2017**, *3*, e1700732.

[31] Kahnamouei, M. H.; Shahrokhian, S. Mesoporous Nanostructured Composite Derived from Thermal Treatment CoFe Prussian Blue Analogue Cages and Electrodeposited NiCo-S as an Efficient Electrocatalyst for an Oxygen Evolution Reaction. *Acs Appl. Mater. Inter.* **2020**, *12*, 16250-16263.

[32] Li, W. G.; Wang, H. L. Oligomer-assisted synthesis of chiral polyaniline nanofibers. *J. Am. Chem. Soc.* **2004**, *126*, 2278-2279.

[33] Yin, L. X.; Dou, H.; Wang, A. X.; Xu, G. Y.; Nie, P.; Chang, Z.; Zhang, X. G. A functional interlayer as a polysulfides blocking layer

for high-performance lithium-sulfur batteries. *New J. Chem.* **2018**, *42*, 1431-1436.

[34] Lu, Y. H.; Wang, L.; Cheng, J. G.; Goodenough, J. B. Prussian blue: a new framework of electrode materials for sodium batteries. *Chem. Commun.* **2012**, *48*, 6544-6546.

[35] Wang, W. J.; Zhang, Q. H.; Li, J. L.; Liu, X.; Wang, L. J.; Zhu, J. J.; Luo, W.; Jiang, W. An efficient thermoelectric material: preparation of reduced graphene oxide/polyaniline hybrid composites by cryogenic grinding. *Rsc Adv.* **2015**, *5*, 8988-8995.

[36] Bilal, S.; Shah, A. A.; Holze, R. Spectroelectrochemistry of poly(o-phenylenediamine): Polyaniline-like segments in the polymer structure. *Electrochim. Acta.* **2011**, *56*, 3353-3358.

[37] Wang, L. M.; Yao, Q.; Bi, H.; Huang, F. Q.; Wang, Q.; Chen, L. D. PANI/graphene nanocomposite films with high thermoelectric properties by enhanced molecular ordering. *J. Mater. Chem. A.* **2015**, *3*, 7086-7092.

[38] Wang, M. S.; Wang, Z. Q.; Chen, Z.; Yang, Z. L.; Tang, Z. L.; Luo, H. Y.; Huang, Y.; Li, X.; Xu, W. One dimensional and coaxial polyaniline@tin dioxide@multi-wall carbon nanotube as advanced conductive additive free anode for lithium ion battery. *Chem. Eng.*

2018, 334, 162-171.

[39] Bai, M. H.; Liu, T. Y.; Luan, F.; Li, Y.; Liu, X. X. Electrodeposition of vanadium oxide-polyaniline composite nanowire electrodes for high energy density supercapacitors. *J. Mater. Chem. A*. **2014**, 2, 10882-10888.

[40] Huang, J. H.; Wang, Z.; Hou, M. Y.; Dong, X. L.; Liu, Y.; Wang, Y. G.; Xia, Y. Y. Polyaniline-intercalated manganese dioxide nanolayers as a high-performance cathode material for an aqueous zinc-ion battery. *Nat Commun*. **2018**, 9, 2906.

[41] Li, G. C.; Li, G. R.; Ye, S. H.; Gao, X. P. A Polyaniline-Coated Sulfur/Carbon Composite with an Enhanced High-Rate Capability as a Cathode Material for Lithium/Sulfur Batteries. *Adv. Energy Mater*. **2012**, 2, 1238-1245.

[42] Chang, C. H.; Chung, S. H.; Manthiram, A. Ultra-lightweight PANiNF/MWCNT-functionalized separators with synergistic suppression of polysulfide migration for Li-S batteries with pure sulfur cathodes. *J. Mater. Chem. A*. **2015**, 3, 18829-18834.

[43] Ru, Y.; Zheng, S. S.; Xue, H. G.; Pang, H. Potassium cobalt hexacyanoferrate nanocubic assemblies for high-performance aqueous

aluminum ion batteries. *Chem. Eng.* **2020**, 382, 122853.

[44] Tubtimkuna, S.; Krittayavathananon, A.; Chiochan, P.; Duangdangchote, S.; Wutthiprom, J.; Limtrakul, J.; Sawangphruk, M. Polyaniline-grafted hydrolysed polyethylene as a dual functional interlayer/separator for high-performance Li-S@C core-shell batteries. *Chem. Commun.* **2019**, 55, 14263-14266.

[45] Chen, C.; Yan, D.; Luo, X.; Gao, W. J.; Huang, G. J.; Han, Z. W.; Zeng, Y.; Zhu, Z. H. Construction of Core-Shell NiMoO₄@Ni-Co-S Nanorods as Advanced Electrodes for High-Performance Asymmetric Supercapacitors. *Acs Appl. Mater. Inter.* **2018**, 10, 4662-4671.

[46] Gao, L.; Han, E. S.; He, Y. Z.; Du, C. Y.; Liu, J. B.; Yang, X. Effect of different templating agents on cobalt ferrite (CoFe₂O₄) nanomaterials for high-performance supercapacitor. *Ionics.* **2020**, 26, 3643-3654.

[47] Zhang, K. Q.; Lee, T. H.; Cha, J. H.; Varma, R. S.; Choi, J. W.; Jang, H. W.; Shokouhimehr, M. Cerium Hexacyanocobaltate: A Lanthanide-Compliant Prussian Blue Analogue for Li-Ion Storage. *Acs Omega.* **2019**, 4, 21410-21416.

[48] Zhu, L. W.; Liu, N.; Lv, X. C.; Zhang, Z. Q.; Yu, L. M.; Li, X. A

novel metal-organic framework derived carbon nanoflower with effective electromagnetic microwave absorption and high-performance electrochemical energy storage properties. *Chem. Commun.* **2021**, 57, 2539-2542.

[49] Wang, Z. Y.; Wang, L.; Liu, S.; Li, G. R.; Gao, X. P. Conductive CoOOH as Carbon-Free Sulfur Immobilizer to Fabricate Sulfur-Based Composite for Lithium-Sulfur Battery. *Adv. Funct. Mater.* **2019**, 29, 1901051.

[50] Yeon, J. S.; Park, S. H.; Suk, J.; Lee, H.; Park, H. S. Confinement of sulfur in the micropores of honeycomb-like carbon derived from lignin for lithium-sulfur battery cathode. *Chem. Eng.* **2020**, 382, 122946.

국 문 초 록

고 에너지 밀도 및 수명이 긴 리튬-황 배터리를 추구하기 위해서는 리튬 폴리 설퍼이드의 셔틀 효과를 억제하는 것이 매우 중요하다. 이 연구에서, 중공성 코발트-철 프러시안 블루 아날로그 나노큐브는 배향 부착 합성방법을 통해 얻어졌다. 얻어진 코발트-철 프러시안 블루 아날로그 나노큐브의 표면에 폴리 아닐린을 추가로 코팅 하였고, 성능 평가를 위해 폴리 프로필렌 분리막 표면을 폴리 아닐린 코팅된 중공성 코발트-철 프러시안 블루 아날로그 나노큐브 물질로 개질하여 리튬-황 배터리 연구를 진행하였다. 황이 60 % 로 올라간 양극재를 사용하여 리튬-황 배터리에 적용해본 결과, 주사 전류 밀도 1 A g^{-1} 에서 초기용량은 723 mA h g^{-1} 을 나타냈다. 이러한 리튬-황 배터리는 주사 전류밀도 1 A g^{-1} 에서 100회 충·방전 후 83.5 % 의 용량을 나타냈고, 쿨롱효율은 모든 100회 충·방전 과정 동안 99.5 % 이상으로 유지되었다. 이는 분리막을 통한 리튬이온의 흡수나 방해가 없어 이온 전달에 용이하며 리튬 폴리설퍼이드가 음극으로 이동하는 것을 방지하는 효율적인 이온 체가 있음을 나타낸다. 본 연구에서 얻어진 결과는, 폴리 아닐린 코팅된 중공성 코발트-철 프러시안 블루 아날로그 나노큐브 물질이 리튬-황 배터리의 성능을 더욱 향상시킬 수 있는 잠재력을 보여주었다.

주요어: 리튬-황 배터리, 분리막, 중공성 코발트-철 프러시안
블루 아날로그 나노 큐브, 폴리아닐린

학 번: 2019-26495